THE JOURNAL OF BIOLOGICAL CHEMISTRY VOL. 291, NO. 5, pp. 2499–2509, January 29, 2016
Published in the U.S.A.

Mechanisms of Calmodulin Regulation of Different Isoforms of Kv7.4 K^+ Channels*

Received for publication, May 27, 2015, and in revised form, October 21, 2015 Published, JBC Papers in Press, October 29, 2015, DOI 10.1074/jbc.M115.668236

Choong-Ryoul Sihn[‡], Hyo Jeong Kim[§], Ryan L. Woltz[§], Vladimir Yarov-Yarovoy[¶‖], Pei-Chi Yang[**], Jun Xu[‡‡], Colleen E. Clancy[**], Xiao-Dong Zhang[§‖], Nipavan Chiamvimonvat[§‖], and Ebenezer N. Yamoah[‡1]

*From the [‡]Department of Physiology and Cell Biology, Program in Communication Science, School of Medicine, University of Nevada, Reno, Reno, Nevada 85997, the [§]Department of Internal Medicine, Division of Cardiovascular Medicine, [¶]Department of Physiology and Membrane Biology, and **Department of Pharmacology, University of California, Davis, Davis, California 95616, the [‖]Northern California Health Care System, Department of Veterans Affairs, Mather, California 95655, and the [‡‡]Department of Engineering Technology, College of Science and Technology, Tarleton State University, Stephenville, Texas 76402*

Calmodulin (CaM), a Ca^{2+}-sensing protein, is constitutively bound to IQ domains of the C termini of human Kv7 (hKv7, KCNQ) channels to mediate Ca^{2+}-dependent reduction of Kv7 currents. However, the mechanism remains unclear. We report that CaM binds to two isoforms of the hKv7.4 channel in a Ca^{2+}-independent manner but that only the long isoform (hKv7.4*a*) is regulated by Ca^{2+}/CaM. Ca^{2+}/CaM mediate reduction of the hKv7.4*a* channel by decreasing the channel open probability and altering activation kinetics. We took advantage of a known missense mutation (G321S) that has been linked to progressive hearing loss to further examine the inhibitory effects of Ca^{2+}/CaM on the Kv7.4 channel. Using multidisciplinary techniques, we demonstrate that the G321S mutation may destabilize CaM binding, leading to a decrease in the inhibitory effects of Ca^{2+} on the channels. Our study utilizes an expression system to dissect the biophysical properties of the WT and mutant Kv7.4 channels. This report provides mechanistic insights into the critical roles of Ca^{2+}/CaM regulation of the Kv7.4 channel under physiological and pathological conditions.

The Ca^{2+}-binding protein calmodulin (CaM)[2] exemplifies one critical player within the massive interactome of proteins that sculpt Ca^{2+}-dependent signaling as diverse as cellular motility, gene transcription, and ion channel regulation (1–6). Indeed, alterations in protein-protein interactions may result in human genetic diseases (7, 8). CaM often mediates its functions by interacting with the IQ/CaM binding domains (CaMBDs) of target proteins, which have varying consensus sequences that bind to apoCaM and/or calcified CaM with K_ds in subnanomolar concentrations (6, 9, 10). Local placement of Ca^{2+} sensors allows swift and efficient Ca^{2+} signaling, whereas global Ca^{2+} promotes the integration of Ca^{2+}-mediated functions (3). An example is the tethering of CaM to Ca^{2+} channels, which serve as the Ca^{2+} source (11, 12). However, in instances where the target protein does not constitute the Ca^{2+} source, (*e.g.* Ca^{2+}/CaM regulation of Na^+ and K^+ channels) (4, 13), the Ca^{2+}-sensing mechanisms are unclear.

Kv7 (KCNQ) channels are expressed in a tissue-specific manner to regulate neuronal and cardiac excitability (5, 14). Additionally, K^+ extrusion through Kv7 channels is necessary to generate the endocochlear potential to support hair cell (HC) functions in the inner ear (15–17). Because of their critical tissue-specific functions, mutations and malfunctions of Kv7 channels lead to epileptic and arrhythmia syndromes (18). Mutations in Kv7.4 (KCNQ4) channels lead to autosomal-dominant, progressive, high-frequency hearing loss, denoted as non-syndromic DFNA2 (19, 20).

In the mouse inner ear, there are at least four functionally distinct splice variants of Kv7.4 that have been identified to be expressed differentially in HCs and spiral ganglion neurons (SGNs) and whose altered expression has been implicated as the potential mechanism for the disease (21, 22). A prominent difference between the splice variants of the human Kv7.4 (hKv7.4) occurs at the C termini, where CaMBDs and the coiled-coil domain for subunit oligomerization are featured (18, 23–25).

The hKv7.4 consists of two major isoforms, *a* and *b*, that contain two putative CaMBDs (10). Additionally, the *a* isoform has a third CaMBD at the C terminus. The Ca^{2+}-sensing domain for the Kv7.4/CaM complex is not well defined, although earlier studies have suggested that the N lobe is the Ca^{2+} sensor (10). Here we utilize an expression system to systematically determine the Ca^{2+}/CaM regulation of the two distinct isoforms of hKv7.4. Moreover, because a known *DFNA2* missense mutation (G321S) lies upstream of the CaMBD, we tested the hypothesis that the missense mutation may alter the inhibitory effects of Ca^{2+}/CaM on the Kv7.4 channel.

Multidisciplinary techniques were used, including patch clamp recordings, biochemical studies, and molecular modeling. Insights into these existing gaps in our knowledge may provide an important framework for understanding how mutations result in autosomal-dominant, progressive, high-fre-

* This work was supported by National Institutes of Health Grants R01 DC0100386, R01 DC007592, and DC003826 (to E. N. Y.); R01 HL085844 and R01 HL085727 (to N. C.); and R01 HL085844-S1 (to R. L. W.). This work was also supported by Department of Veterans Affairs Merit Review Grant I01BX000576 (to N. C.) and American Heart Association Western States Beginning Grant-in-Aid 14BGIA18870087 (to X. D. Z.). The authors declare that they have no conflicts of interest with the contents of this article. The content is solely the responsibility of the authors and does not necessarily represent the official views of the National Institutes of Health.

[1] To whom correspondence should be addressed: Program in Communication Science, Dept. of Physiology and Cell Biology, University of Nevada Reno, Reno, NV. E-mail: enyamoah@gmail.com.

[2] The abbreviations used are: CaM, calmodulin; CaMBD, calmodulin binding domain; HC, hair cell; SGN, spiral ganglion neuron; MT, mutant; EGFP, enhanced green fluorescent protein; DN, dominant negative; pF, picofarad.

quency hearing loss and, possibly, for the development of strategies to alleviate the symptoms of the disease.

Experimental Procedures

Generation of Mutant (MT) Forms of hKv7.4 (hKCNQ4) and Epitope-tagged Constructs—WT hKv7.4 clones, isoform *a* (695 amino acids, gene ID NM_004700) and isoform *b* (641 amino acids, gene ID NM_172163), were purchased from Qiagen (Valencia, CA). The coding sequences were subcloned into the pIRES2-EGFP plasmid vector (Clontech, Mountain View, CA). Isoleucine and glutamine residues in the IQ domain were substituted by valine and alanine residues to generate IQ mutant channels in WT hKv7.4 (isoform *a* and *b*) clones (26) using the QuikChange II mutagenesis kit (Stratagene, La Jolla, CA) and verified by automated sequencing. A missense mutation, G321S, has been shown previously to cause progressive hearing loss (27). The mutant G321S channel ($Kv7.4_{G321S}$) was generated in the WT hKv7.4 (isoform *a*). pIRES2-EGFP-hKv7.4-WT and mutants were used in electrophysiologic recordings and biochemical studies. We used EGFP expression as a transfection marker.

To study the subcellular localization of WT and MT subunits, two different epitopes, modified HA and c-Myc tags, were inserted into the pCMV-hKv7.4-WT and MT constructs in which the EGFP genes were eliminated. Modified HA and c-Myc epitopes were flanked with the ClC-5 chloride channel D1-D2 loop to increase accessibility and inserted in the end of the S1-S2 loop of hKv7.4, as described previously, in the Kv7.2/7.3 (28) and Kv7.4 (29) channels. S1-S2 loop amino acid sequences were changed to STIQEHQELANENSEH**YPYDVPDYA**VTFEERDKCPEWNC for HA-tagged constructs and STIQEHQELANENSEH-**EQKLISEEDL**VTFEERDKCPEWNC for c-Myc tagged constructs. The inserted regions are underlined, and epitopes are shown in boldface. Epitope tags were generated by recombination polymerase chain reaction and verified by automated sequencing.

Heterologous Expression, Tissue Culture, and Transfection—Plasmids (pJG60 and pGJ65) containing CaM and DN MT of CaM (CaMDN) were obtained from Dr. Trisha Davis (University of Washington, Seattle, WA). CaMDN has alanine substitutions of each of the four aspartates in the Ca^{2+}-binding EF hands (D20A, D56A, D93A, and D129A) (30). CHO cells were obtained from the ATCC. CHO cells were maintained in F12-K containing 10% fetal bovine serum (Invitrogen). Cell cultures were kept at 37 °C in a 5% CO_2 incubator. The cells were trypsinized, plated at a concentration of 1.5×10^5 cells/ml in 2 ml of culture medium in 35-mm dishes, and transfected with 1 μg of total DNA/dish. Transfections were performed using Lipofectamine following the protocol of the manufacturer (Invitrogen). The cells were rinsed in fresh culture medium and incubated for 24 h before patch clamp recordings. Transfected cells were identified for recording by visualization of the EGFP co-expression (BD Biosciences, Clontech).

Immunoprecipitation—CHO cells expressing either Kv7.4a or Kv7.4b were lysed in radioimmune precipitation assay buffer (50 mM Tris-HCl (pH 8), 150 mM NaCl, 1% Nonidet P-40, 200 μM Na_3VO_4, 0.5% sodium deoxicholate, 0.1% SDS, and protease inhibitor mixture tablets (Roche)). Cell lysates were mixed with protein A-Sepharose beads (Roche) for preclearing and incubated with anti-Kv7.4 antibody (Neuromab) and 2 mM of EGTA or $CaCl_2$ overnight at 4 °C. Immune complexes were pulled down with beads and washed three to four times with radioimmune precipitation assay buffer. Immunoprecipitated proteins were separated by SDS-PAGE and blotted onto nitrocellulose filters after adding protein loading dye and boiled for 5 min. Blocking was performed at room temperature for 1 h in TBS with 5% nonfat milk, followed by incubation with anti-Kv7.4 (1:500 dilution) and anti-CaM (1:1000 dilution) antibodies in TBS. After washing with TBS, the membranes were incubated with horseradish peroxidase-conjugated secondary antibodies. Proteins were visualized using an enhanced chemiluminescence kit (Thermo Scientific, Pittsburgh, PA).

CaM Binding Site Prediction—Kv7.4*a* and *b* protein sequences (NP_004691.2) were used to predict CaM binding sites by using web-based tools from a CaM target database.

Electrophysiology—All electrophysiological experiments were performed at room temperature (21–22 °C). Reagents were obtained from Sigma-Aldrich (St. Louis, MO) unless specified otherwise. Ca^{2+} concentrations were determined using custom-written software.

Whole-cell and cell-attached single-channel voltage clamp recordings were performed on CHO cells using an Axopatch 200B amplifier (Molecular Devices, Sunnyvale, CA). Current traces were amplified, filtered (bandpass, 2–10 kHz), and digitized at 5–500 kHz using an analog-to-digital converter, Digidata 1322A (Molecular Devices), as described earlier (26). Fire-polished electrodes (3–5 MΩ) were pulled from borosilicate glass. Several basic criteria were set to ensure optimum quality of recordings and acceptance of data, including the following: initial stable seals for at least 5 min before recordings, elimination of cells with current traces that exhibit signs of voltage inhomogeneities, and exclusion of cells with more than 20% change in series resistance before and during recordings.

Whole-cell K^+ current amplitudes at varying test potentials were measured at the peak and steady-state levels using a peak and steady-state detection routine. The current magnitude was divided by the cell capacitance (picofarad) to generate the current density-voltage relationship. For single-channel recordings, leakage and capacitative transient currents were subtracted by fitting a smooth template to null traces. Leak-subtracted current recordings were idealized using a half-height criterion. Transitions between closed and open levels were determined using a threshold detection algorithm that required that two data points exist above the half-mean amplitude of the single-unit opening. The computer-detected openings were confirmed by visual inspection, and sweeps with excessive noise were discarded. Amplitude histograms at a given test potential were generated and then fitted to a single Gaussian distribution using a Levenberg-Marquardt algorithm to obtain the mean ± S.D. At least four voltage steps and their corresponding single-channel currents were used to determine the unitary conductance. Single-channel current-voltage relations were fitted by linear least square regression lines, and single-channel conductances were obtained from the slope of the regression lines. Idealized

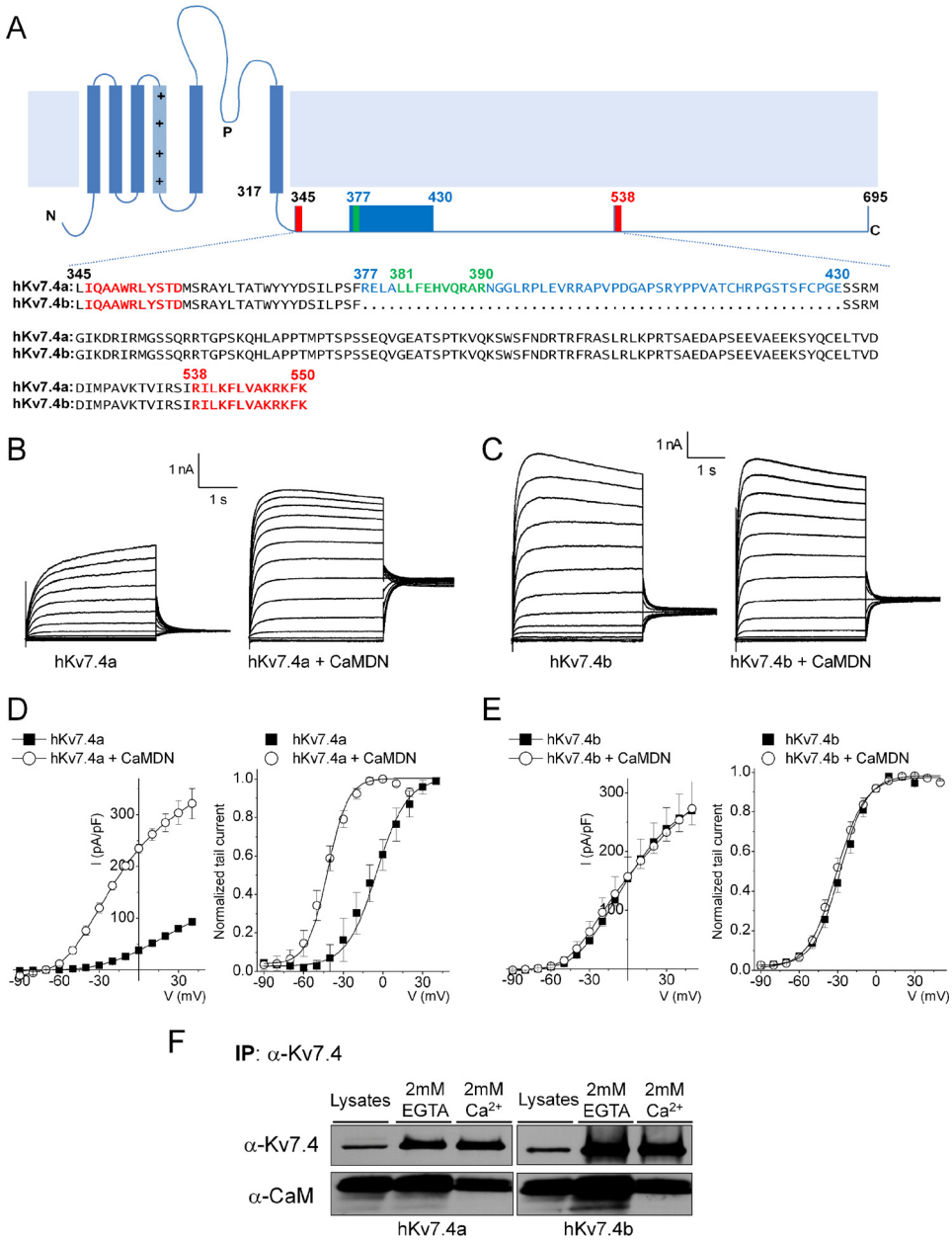

FIGURE 1. **The CaMBD linker is required for the Ca^{2+}/CaM-dependent inhibition of the Kv7.4 current.** *A*, schematic of the Kv7.4 α-subunit structure. The C-terminal sequence alignment of the two isoforms (hKv7.4*a*, NP_004691; hKv7.4*b*, NP_751895) is shown. Two known CaM binding domains ($CaMBD_A$ and $CaMBD_B$) are marked in *red*, and a putative CaMBD is marked in *green*. Spliced alteration of hKv7.4 (hKv7.4a *versus* hKv7.4b) is indicated in *blue*. *B* and *C*, representative traces showing whole-cell recordings from CHO cells transfected with hKv7.4*a* and hKv7.4*b* and co-transfected with either empty vector or CaMDN. The current traces were recorded from a holding potential of −70 mV to step potentials ranging from −90 to 40 mV using voltage increments of 10 mV. Tail currents were recorded at −30 mV. *D* and *E*, plots of current density (picoampere/picofarad)-voltage relations of currents (*left*) were derived from CHO cells expressing hKv7.4*a* (or hKv7.4*b*) (*closed squares*, $n = 21$) and hKv7.4*a* (or hKv7.4*b*) + CaMDN (*open circles*, $n = 21$). Normalized tail currents of hKv7.4*a* and hKv7.4*a* + CaMDN are plotted against the applied voltage to generate the activation curves (*right*), which were fitted with a Boltzmann function. The half-activation voltages ($V_{½}$, in millivolt) and slope factor, k, for hKv7.4*a* were as follows: −5.7 ± 1.1 and 14.1 ± 0.9 ($n = 17$); for hKv7.4*a* + CaMDN they were −42.0 ± 1.8 and 11.4 + 1.5 ($n = 19$), respectively. The $V_{½}$ and k values for hKv7.4*b* were as follows: −28.0 ± 2.6 and 10.5 ± 1.4; and for hKv7.4*b* + CaMDN they were −31.0 ± 1.4 and 11.1 ± 1.0 ($n = 21$). *F*, CHO cells were expressed with either hKv7.4*a* or hKv7.4*b* for 24 h. After preparation of cell lysates, immunoprecipitation (*IP*) was accomplished using hKv7.4 antibody with a buffer containing either 2 mM of $CaCl_2$ or EGTA. Association of hKv7.4 with CaM is Ca^{2+}-independent.

records were used to construct ensemble-averaged currents, open probability, and histograms for the distributions of open and closed intervals.

Structural Modeling of the hKv7.4 Channel—We used Rosetta applications (27, 31–36) and the open-state structure of the rKv1.2 pore-forming domain (PDB code 2R9R) (37) to generate structural models of the hKv7.4 WT and G321S MT channels. Residues around the Kv7.4 Ala-263 residue (insertion in the S5 P-helix loop compared with the rKv1.2 template sequence) and 100 residues of the C terminus (that included CaMBD A and B regions) were modeled *de novo*. 50,000 models of the hKv7.4 WT and $hKv7.4_{G321S}$ MT channels were generated, and then the 1000 lowest-energy models were clustered as described previously (38). Structural models of the hKv7.4 WT and $hKv7.4_{G321S}$ MT channels shown in this paper represent the center of one of the top ten clusters.

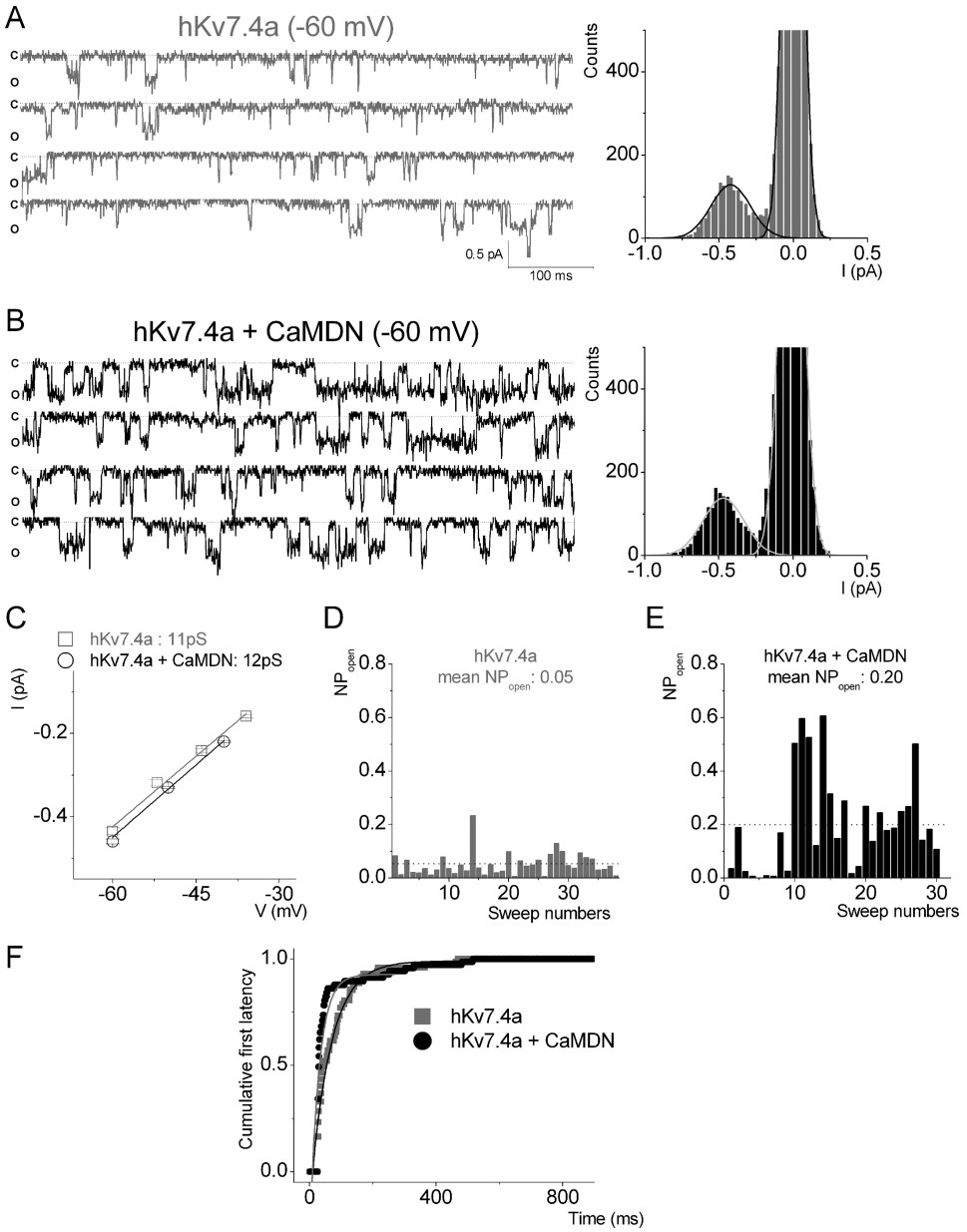

FIGURE 2. **CaMDN increases the open probability but not unitary conductance of the Kv7.4*a* channel.** *A* and *B*, a set of single-channel traces was recorded from CHO cells expressing either hKv7.4*a* alone (*gray*) or hKv7.4*a* + CaMDN (*black*) at a −60 mV step potential. The *dotted lines* represent closed states. Representative amplitude histograms of hKv7.4*a* alone and hKv7.4*a* + CaMDN at −60 mV are shown on the *right*. *c*, closed; *o*, open; *I*, current. *C*, data from amplitude histograms of applied voltages were used to generate current-voltage relationships. The single-channel conductances were 11 ± 0.6 pS ($n = 9$) (hKv7.4*a*) and 12 ± 0.8 pS ($n = 10$) (hKv7.4*a* + CaMDN), respectively. *D* and *E*, the open probability of hKv7.4*a* and hKv7.4*a* + CaMDN. Mean open probabilities are indicated by the *dotted lines*. *F*, exponential fits to the first latency histograms are shown. Time constants of hKv7.4*a* and hKv7.4*a* + CaMDN are indicated in milliseconds, and their median values are 46 ± 6 and 87 ± 9 ms ($n = 7$), respectively.

Statistical Analyses—Where appropriate, pooled data are presented as means ± S.E. Curve fits and data analysis were performed using Origin software (MicroCal Inc.). Statistical comparisons were performed using the statistical package in the Origin software, with $p < 0.05$ considered significant. For multiple comparisons, one-way analysis of variance combined with Tukey test was used. For comparisons between two groups, Student's *t* test was used.

Results

Inhibitory Effects of CaM on the Long Isoform of hKv7.4—Previous studies have documented functionally distinct splice variants of Kv7.4 that are expressed differentially in HCs and SGNs (21, 22). We first examined the sequence alignment of two isoforms, hKv7.4*a* and *b*, as well as the mouse homologues of $Kv7.4_{v1}$ and $Kv7.4_{v4}$, which show stark differential expression in inner ear HCs and SGNs with distinct functional phenotypes (21, 22). The C terminus of hKv7.4*a* contains two CaMBDs, highlighted in *red* in Fig. 1*A* and designated here as $CaMBD_A$ and $CaMBD_B$, respectively. We identified an additional putative CaMBD in the C terminus of hKv7.4*a*, highlighted in *green* in Fig. 1*A*. In contrast, the C terminus of hKv7*b* contains only two CaMBDs, $CaMBD_A$ and $CaMBD_B$ (Fig. 1*A*).

Shown in Fig. 1, *B* and *C*, are whole-cell hKv7.4*a* and *b* current traces. Heterologous expression of Kv7.4*a* and *b* yielded

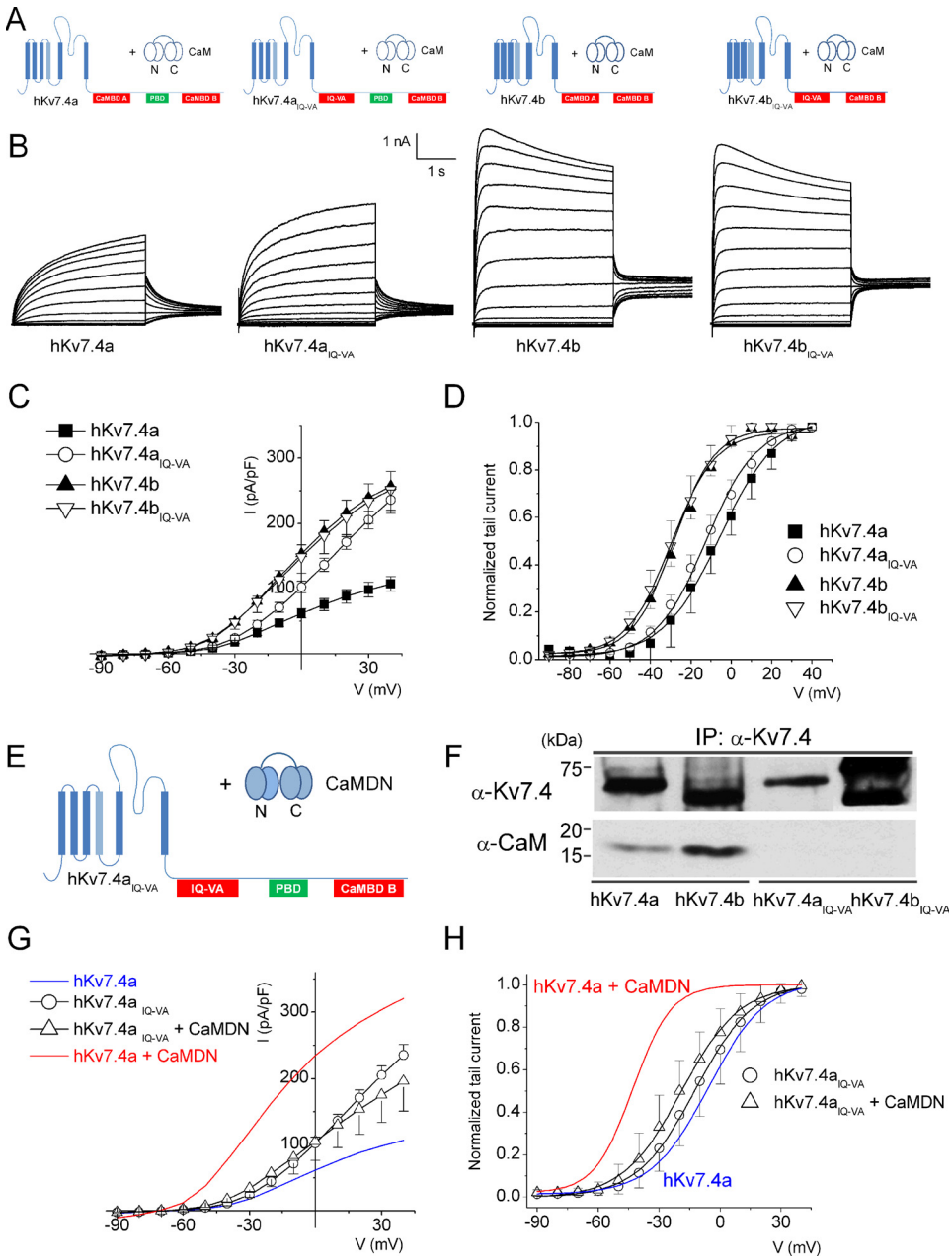

FIGURE 3. **The IQ motif in CaMBD$_A$ is necessary but not sufficient for Ca^{2+}/CaM-dependent inhibition of the hKv7.4 current.** *A*, the combinations of hKv7.4 and MT hKv7.4$_{IQ-VA}$ isoforms with endogenous CaM. *B*, representative current traces of hKv7.4 and hKv7.4$_{IQ-VA}$ recorded from transfected CHO cells. Whole-cell recordings were generated from a holding potential of −70 mV to step potentials ranging from −90 to 40 mV using voltage increments of 10 mV. Tail currents were recorded at −30 mV. *C*, plots of current density (picoampere/picofarad)-voltage relations were generated from CHO cells expressing hKv7.4 and hKv7.4$_{IQ-VA}$ isoforms ($n = 19$). *I*, current. *D*, normalized tail currents of hKv7.4 (hKv7.4$_{IQ-VA}$) isoforms were plotted against applied voltages to generate activation curves that were fitted with the Boltzmann function. The $V_{½}$ (in millivolt) and k values for hKv7.4*a* and hKv7.4a_{IQ-VA} were as follows: −5.7 ± 1.1 and 14.1 ± 0.9 ($n = 17$), and −12.2 ± 0.5 and 11.4 ± 0.5, respectively ($n = 17$). For hKv7.4*b* and hKv7.4b_{IQ-VA}, the $V_{1/2}$ and k values were as follows: −28.4 ± 2.0 and 10.1 ± 1.2 ($n = 17$) and −29.7 ± 1.2 and 10.9 ± 1.0, respectively ($n = 17$). *E*, schematic of the experiment performed with hKv7.4a_{IQ-VA} + CaMDN. *F*, co-immunoprecipitation (*IP*) experiment showing that association of hKv7.4$_{IQ-VA}$ isoforms with CaM was abolished. *G*, current density (in picoampere/picofarad)-voltage relations of hKv7.4a_{IQ-VA} alone and hKv7.4a_{IQ-VA} + CaMDN ($n = 17$). *H*, normalized tail currents for hKv7.4a_{IQ-VA} were plotted against the applied voltage to generate activation curves fitted with a Boltzmann function. The $V_{½}$ (in millivolt) and k values for hKv7.4a_{IQ-VA} were as follows: −12.2 ± 0.5 and 11.4 ± 0.5 ($n = 17$); and for hKv7.4a_{IQ-VA} + CaMDN they were −19.0 ± 0.7 and 11.8 ± 0.7, respectively ($n = 17$). *Blue* and *red curves* denote data from Fig. 1*D* for comparison with hKv7.4a and hKv7.4 + CaMDN, respectively.

voltage-dependent K^+ currents similar to the native current I_{KL} in HCs and SGNs (39–42) (Fig. 1, *B* and *C*). Because CHO cells have endogenous CaM (22), we co-expressed hKv7.4*a* with CaMDN constructs to knock down endogenous CaM effects. The resulting current was ~3-fold greater than the current from hKv7.4*a* alone, and the mid-point of activation ($V_{½}$) was shifted leftward by ~37 mV (Fig. 1*D*). In surprising contrast, expressing hKv7.4*b* alone yielded a current density that was at least ~2-fold larger than hKv7.4*a* but remained insensitive to CaM modulation after co-expression with CaMDN (Fig. 1, *C* and *E*). Indeed, the $V_{½}$ of hKv7.4*b* currents and the current density remained unchanged in the presence of CaMDN (Fig. 1*E*).

We sought to determine whether the two spliced variants form complexes with CaM, a requirement for their interaction.

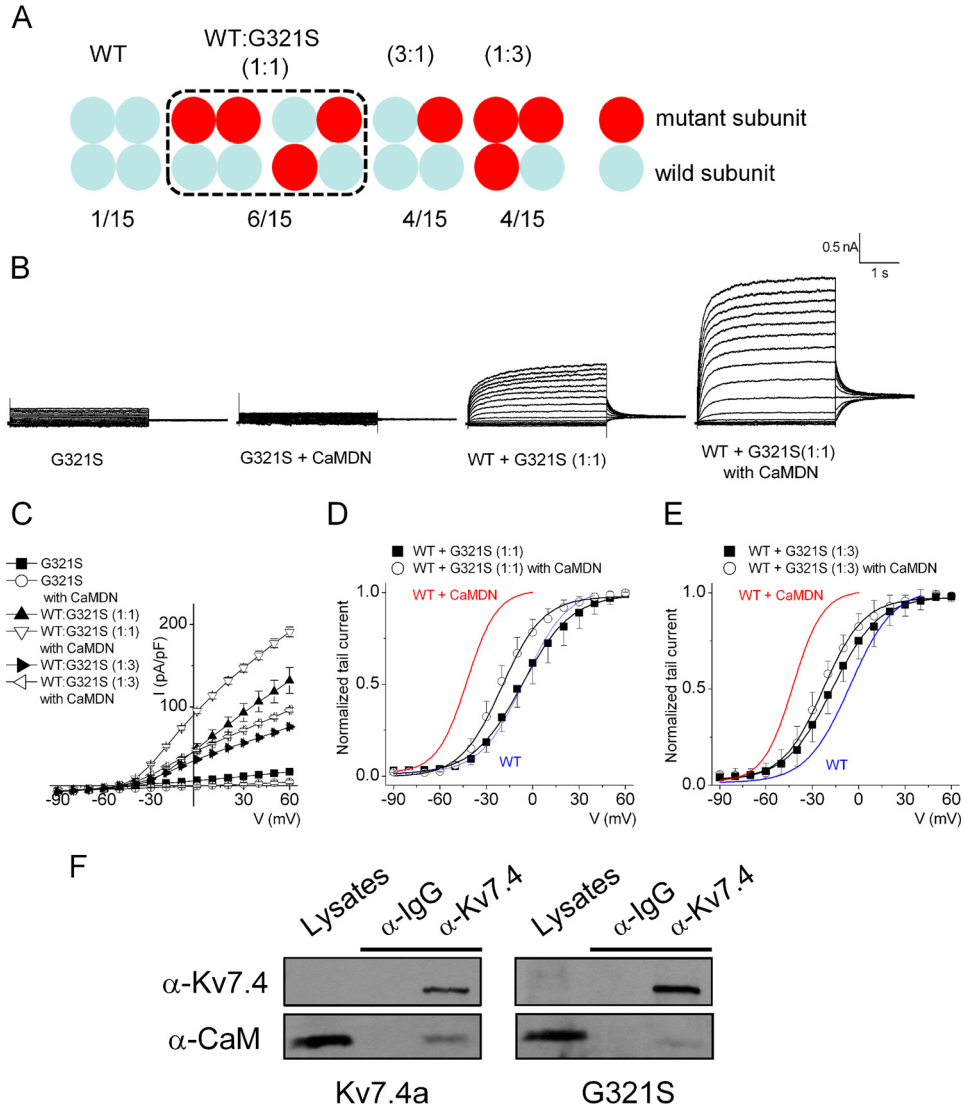

FIGURE 4. **Co-expressing the hKv7.4*a* G321S MT subunit with the WT subunit reduces current density but attenuates the effect of CaMDN on the activation curve.** *A*, schematic of expected channel combinations with hKv7.4*a* WT and G321S MT type subunits. The numbers presented at the *bottom* show the potential membrane-expressed channel populations formed from each different ratio of WT and MT subunit. *B*, representative traces show the whole-cell recording from CHO cells transfected with hKv7.4*a* WT and G321S MT subunits in a 1:1 ratio (WT:G321S) with either empty vector or CaMDN. The current traces were recorded from a holding potential of −70 mV to step potentials ranging from −90 to 60 mV using voltage increments of 10 mV. Tail currents were recorded at −30 mV. *C*, plots of current density (picoampere/picofarad)-voltage relations of currents were derived from CHO cells expressing different combinations of hKv7.4*a* G321S alone, hKv7.4*a* + CaMDN, 1:1 or 1:3 ratio of (WT:G321S) alone, or with CaMDN. *D* and *E*, normalized tail currents of 1:1 ratio (WT:G321S) alone and 1:1 ratio (WT:G321S) + CaMDN are plotted on each voltage applied and generated the activation curves fitted with a Boltzmann function. *Blue* and *red curves* denote data from Fig. 1*D* for comparison with hKv7.4a and hKv7.4 + CaMDN, respectively. *F*, CHO cells were expressed with either hKv7.4*a* or hKv7.4*a* G321S for 24 h. After preparation of cell lysates, immunoprecipitation was accomplished with Kv7.4 antibody to test CaM binding to the channel subunit.

Co-immunoprecipitation experiments indicated that CaM/hKv7.4*a* and *b* form complexes in a Ca^{2+}-independent manner (Fig. 1*F*), similar to the tethering of CaM to Kv7.1–5 and Ca^{2+} channels described previously (1, 5, 14, 18, 22, 43).

Inhibitory Effects of CaM on the Open Probability and the First Latency of Kv7.4a Unitary Currents—To assess the biophysical mechanisms for CaM-dependent modulation of hKv7.4, we recorded single-channel fluctuations in CHO cells expressing hKv7.4*a* alone and in combination with CaMDN (Fig. 2). Co-expression of hKv7.4*a* with CaMDN enhanced the probability of the channel opening by ~4-fold, but the single-channel unitary conductance remained unaffected (Fig. 2, *A–E*). Analyses of the first latency revealed that CaMDN decreased the waiting time to first opening of hKv7.4*a* by ~2-fold (Fig. 2*F*).

An Intact IQ Motif in CaMBD$_A$ Is Required for the Regulation of hKv7.4a—Next, we examined the mechanisms for CaM regulation of hKv7.4 channels by performing site-directed mutagenesis of the IQ motif to valine and alanine residues, respectively, as illustrated in Fig. 3*A*. Expression of hKv7.4$a_{IQ\text{-}VA}$ in CHO cells yielded current densities that were greater than those of control hKv7.4*a* (Fig. 3, *B* and *C*). The current densities at the step voltage of 0 mV for hKv7.4*a* and hKv7.4$a_{IQ\text{-}VA}$ were 62 ± 7 and 102 ± 9 pA/pF, respectively ($p < 0.01$, $n = 19$). In contrast, similar mutations of hKv7.4*b* to hKv7.4$b_{IQ\text{-}VA}$ produced current densities that were statistically unaltered (Fig. 3, *B* and *C*). The current densities at the step voltage of 0 mV for hKv7.4*b* and hKv7.4$b_{IQ\text{-}VA}$ were 150 ± 25 and 155 ± 19 pA/pF, respectively ($p = 0.1$, $n = 19$). The findings from the

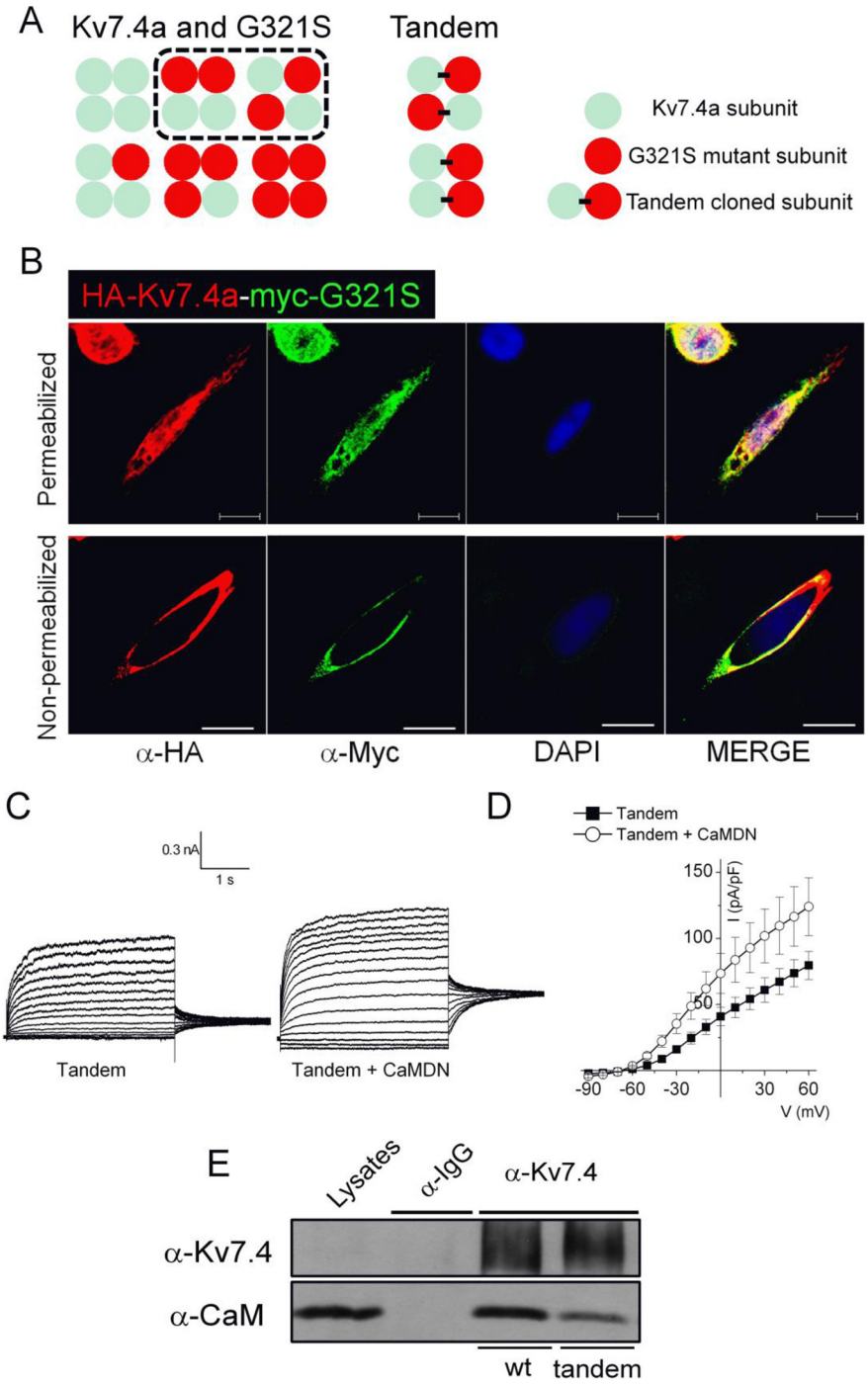

FIGURE 5. **Tandem channel subunits clarify the effect of the MT subunit.** *A*, schematic of expected channel combinations when cells express the hKv7.4 WT and G321S MT subunit or tandem clones. *B*, the tandem clone has two epitopes, HA and myc, located at the extracellular loop between the S1 and S2 transmembrane domains of Kv7.4*a* WT and G321S MT, respectively. Anti-HA and anti-myc antibodies were used for the immunofluorescence assay with the conditions either permeabilized or non-permeabilized. *Scale bars* = 10 μm. *C*, representative traces showing the whole-cell recording from CHO cells transfected with tandem clones alone or with CaMDN. The current traces were recorded from a holding potential of −70 mV to step potentials ranging from −90 to 60 mV using voltage increments of 10 mV. Tail currents were recorded at −30 mV. *D*, plots of current (*I*) density (picoampere/picofarad)-voltage relations of currents were derived from CHO cells expressing tandem clones with either empty vector or CaMDN. *E*, CHO cells were expressed with either hKv7.4*a* or tandem clones for 24 h. After preparation of cell lysates, immunoprecipitation was accomplished with Kv7.4 antibody to test CaM binding to the channel subunit.

current density suggest that an intact IQ motif is required for the observed inhibitory effects of hKv7.4a by CaM.

There were no significant differences in the steady-state voltage-dependent activation between hKv7.4b and hKv7.4b$_{IQ\text{-}VA}$ (the two curves overlapped completely). For hKv7.4a and hKv7.4a$_{IQ\text{-}VA}$, the $V_{1/2}$ was shifted from −5.7 ± 1.1 mV for hKv7.4a to −12.2 ± 0.5 mV for hKv7.4a$_{IQ\text{-}VA}$, an estimated ~6 mV shift to the left. However, the changes were not significant (Fig. 3*D*).

We probed whether the other putative CaMBDs, besides the IQ domain, can confer additional modulation of the channels. We co-expressed hKv7.4$a_{IQ\text{-}VA}$ with CaMDN (Fig.

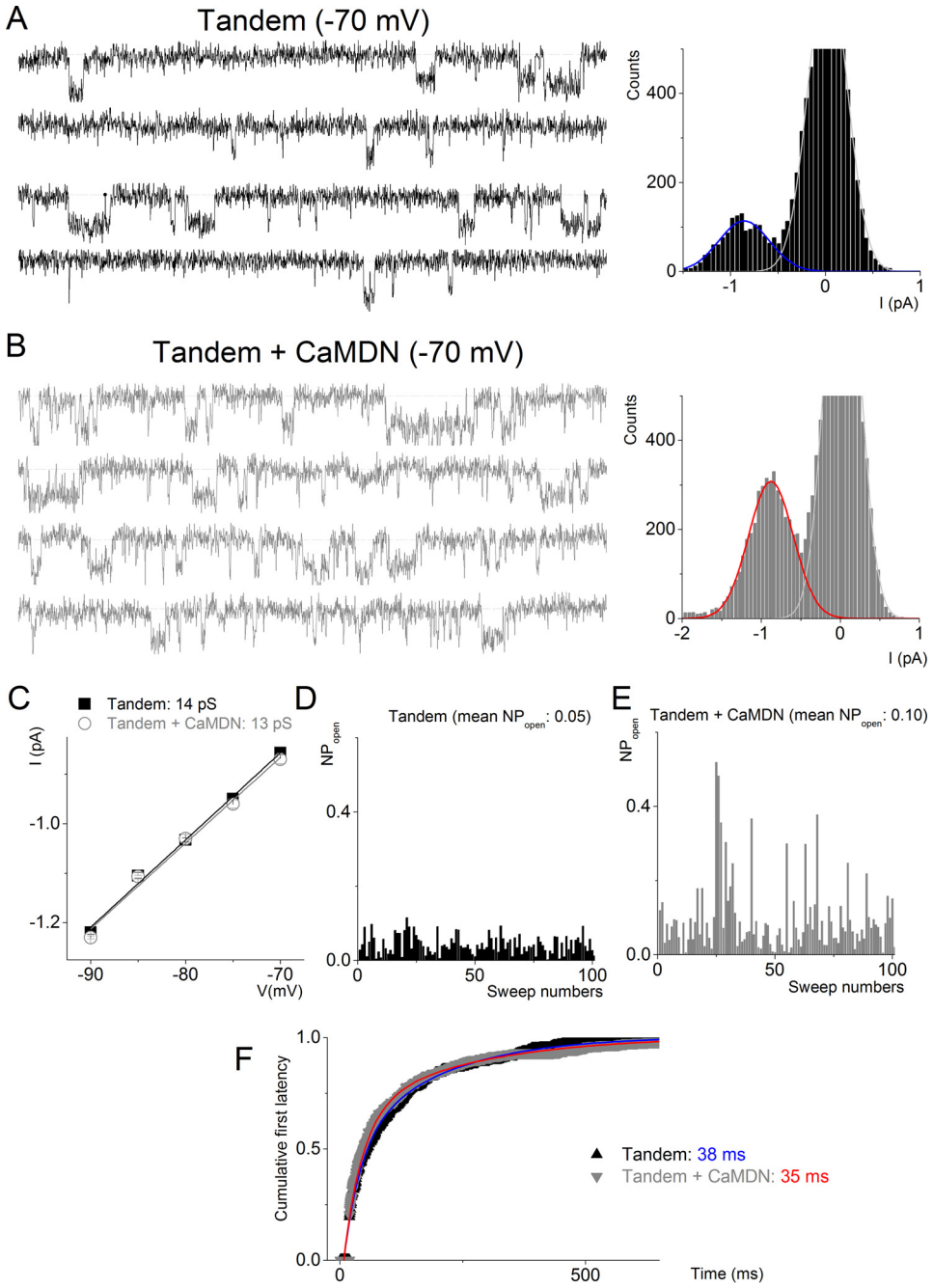

FIGURE 6. **CaMDN increases the open probability but not unitary conductance of tandem-cloned channels.** *A* and *B*, representative sets of single-channel traces were recorded from CHO cells expressed with either Tandem alone (*black*) or Tandem + CaMDN (*gray*) at a −70 mV step potential. The *dotted lines* represent closed states. Amplitude histograms of Tandem + CaMWT and Tandem + CaMDN at −70 mV were fitted with a Gaussian function to find a peak point. *I*, current. *C*, data from amplitude histograms of applied voltages were used to generate current-voltage relationships. The single-channel conductances were 13 ± 0.6 pS ($n = 8$) (Tandem alone) and 13 ± 0.2 ($n = 7$) pS (Tandem + CaMDN), respectively. *D* and *E*, the open probability data were generated from at least 200 sweeps at a specific test potential using recordings from Tandem alone and Tandem + CaMDN. Mean open probabilities are shown at the *top*. *F*, exponential fits to the first latency histograms. Time constants of Tandem alone (*blue*) and Tandem + CaMDN (*red*) are indicated in milliseconds.

3*E*). CaMDN did not produce a sizable increase in current density, nor did it shift the voltage-dependent activation of hKv7.4$a_{\mathrm{IQ\text{-}VA}}$ currents, consistent with the lack of association between hKv7.4$a_{\mathrm{IQ\text{-}VA}}$ with CaM (Fig. 3, *F–H*). These findings suggest the necessity for an intact IQ motif to ensure the regulatory role of the other CaMBDs (1).

Ca^{2+}-dependent Modulation of Kv7 Channels in a Disease-causing MT—A previous study has provided evidence that patients with a missense mutation of G321S (glycine-to-serine mutation at position 321) suffer from progressive hearing loss (27). Because the residue Gly-321 lies within the C terminus and is upstream of the $\mathrm{CaMBD_A}$, we took advantage of this known mutation to further examine the inhibitory effects of Ca^{2+}/CaM on the Kv7.4 channel. Site-directed mutagenesis was used to generate the mutation in the Kv7.4 isoform *a* ($\mathrm{Kv7.4_{G321S}}$) and the mutant subunit was co-expressed with hKv7.4*a* WT subunits. Fig. 4*A* outlines the possible combinatorial assembly of a tetrameric channel. Neither the MT chan-

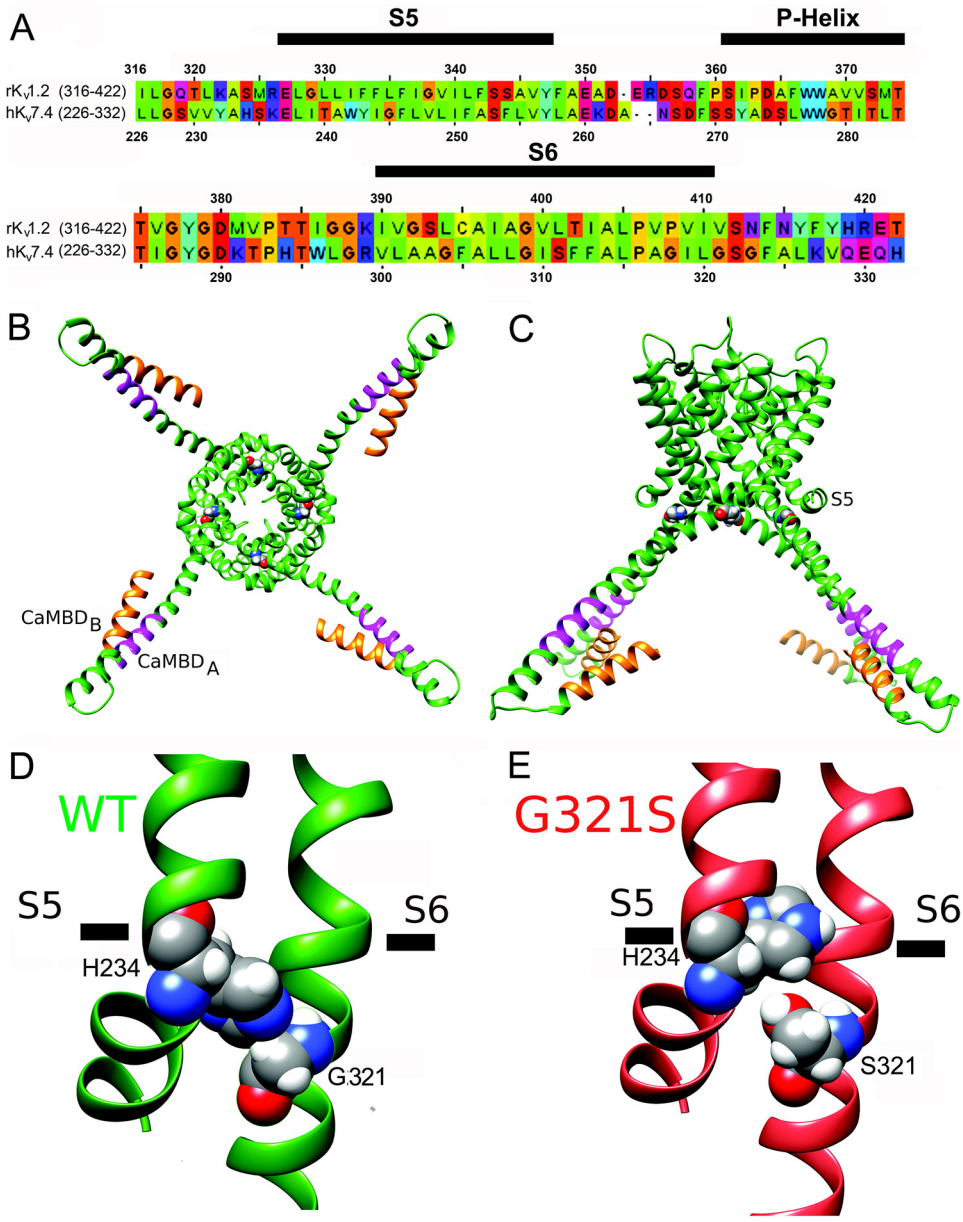

FIGURE 7. **Structural modeling of pore-forming domains and CaMBDs in the hKv7.4 WT and G321S MT.** *A*, sequence alignment of the pore-forming domains of the hKv7.4 and rKv1.2 channels. The S5, P-helix, and S6 regions from the same subunit are marked by *black bars* above the sequence. *B*, structural model of the hKv7.4 WT viewed from the intracellular side of the membrane. The CaMBD A and B regions in the C terminus are colored *orange* and *magenta*, respectively. Gly-321 is shown in spacefilling representation. *C*, transmembrane view of the hKv7.4 model shown in *B*. *D*, close-up view of the structural model of the hKv7.4 WT. Gly-321 and His-234 are shown in spacefilling representation and labeled. *E*, close-up view of the structural model of the hKv7.4 G321S MT.

nel nor addition of CaMDN yielded measurable currents (Fig. 4*B*, *first* and *second panels*). These findings are in keeping with a previous report that determined that Kv7.4$_{G321S}$, when expressed alone, had impaired membrane trafficking. However, co-expression of the MT with the WT subunits facilitated membrane trafficking of the MT subunits (26). As shown in Fig. 4*B* (*third* and *fourth panels*), expression of Kv7.4$_{G321S}$:Kv7.4 (at a 1:1 ratio) yielded a detectable current that was enhanced significantly in the presence of CaMDN (Fig. 4*C*). Analyses of the voltage-dependent activation of the tail currents revealed CaMDN-mediated leftward shifts in the $V_{1/2}$ of activation, consistent with CaM modification of the ensuing heteromeric channel assembly (Fig. 4, *D* and *E*). However, compared with homomeric WT subunits, currents expressed from Kv7.4$_{G321S}$ and Kv7.4 WT subunits exhibited smaller leftward shifts in the voltage-dependent activation (Fig. 4*D*-E). Co-immuno-precipitation experiments of CaM binding to the WT Kv7.4 and Kv7.4$_{G321S}$ subunits revealed weak binding of the mutant subunit to CaM (Fig. 4*F*).

To further test the functionality of Kv7.4:Kv7.4$_{G321S}$ heteromeric channels, we generated tandem Kv7.4:Kv7.4$_{G321S}$ subunits (Fig. 5*A*) with HA and c-Myc tags for Kv7.4 and Kv7.4$_{G321S}$ subunits, respectively. We first assessed whether channels formed from the tandem subunits were expressed on the plasma membrane and identified the expression of the tandem channels using anti-HA and anti-c-Myc antibodies under non-permeabilized conditions (Fig. 5*B*). Expression of the tandem Kv7.4: Kv7.4$_{G321S}$ subunit yielded outward K^+ currents that were enhanced upon co-expression with CaMDN (Fig. 5, *C*

and *D*). The co-immunoprecipitation experiments shown in Fig. 5*E* suggested that CaM binds more weakly with the tandem channel than the WT channel. At the single-channel level, CaMDN increased the probability of the channel opening without altering the unitary conductance (Fig. 6).

Structural Modeling of the hKv7.4 WT and G321S MT—To start exploring the experimental data on the G321S MT channel from a structural perspective, we generated preliminary structural models of the hKv7.4 WT and G321S MT channels as described under "Experimental Procedures." Fig. 7*A* shows the sequence alignment between the pore-forming domains of hKv7.4 channel and the rKv1.2 channel that was used as a template. Our modeling suggests that, in the WT Kv7.4 model (Fig. 7, *B–D*), native Gly-321 (in the S6 segment) allows the side chain of His-234 (in the S4-S5 linker) to come in direct contact with S6 and potentially stabilize a conformation of the C-terminal structure that favors the binding by CaM. In contrast, in the $Kv7.4_{G321S}$ mutant model, the side chain of Ser-321 displaces the side chain of His-234 (in the S4-S5 linker) from its direct interaction with S6 observed in the WT model (Fig. 7*E*). On the basis of our model, the absence of a measurable current in the $Kv7.4_{G321S}$ mutant (Fig. 4*B*) can be explained by the decoupling of the S4-S5 linker-S6 segment interaction that plays a key role in voltage-gated ion channel gating (37, 44–46). Decoupling of the S4-S5 linker-S6 segment interaction can also affect the conformation of the C terminus, which may, in turn, affect CaM binding to the CaMBD region, as demonstrated by our experiments. However, predictions from our structural models will need to be tested in future studies.

Discussion

Kv7 channels underlie the neuronal M current and are constituents of the low voltage-activated K^+ channels in auditory and vestibular HCs and neurons, where they enhance temporal fidelity and control the regularity of trains of spikes to sculpt the coding of information (39, 42, 47, 48). Here we demonstrate that CaM binds to two different isoforms of hKv7.4 channel in a Ca^{2+}-independent manner but that only the long isoform (Kv7.4*a*) is down-regulated by CaM. Ca^{2+}/CaM mediate reduction of hKv7.4*a* currents by decreasing the channel open probability and altering activation kinetics. We demonstrate that G321S, a known missense mutation linked to progressive hearing loss, may destabilize CaM binding, leading to a decrease in the inhibitory effects of Ca^{2+} on the channels.

The hKv7.4 CaMBD-Ca^{2+} Complex—The co-immunoprecipitation data suggest that CaM binds to both isoforms of hKv7.4 in a Ca^{2+}-independent manner. Because of the abundance of CaM in cells, the outcome of the immunoprecipitation assay may be due to the nonspecific bindings from CaM. To directly test the specific binding of hKv7.4 and CaM, we generated the $hKv7.4a_{IQ\text{-}VA}$ mutant channel. As demonstrated in Fig. 3*F*, co-immunoprecipitation of the $hKv7.4a_{IQ\text{-}VA}$ mutant channel failed to pull down CaM. The findings suggest that the observed association of WT hKv7.4 to CaM is not due to the nonspecific bindings from the abundance of CaM in the cells.

One surprising aspect of this finding is that the binding of CaM to isoform *b*, which contains two CaM-binding motifs separated by 127 residues, appears to be functionally inconsequential. In stark contrast to Kv7.1–3 and 5, which also harbor two CaM-binding motifs in the intracellular C terminus separated by ~135 residues (1), CaM interaction with these channels confers functional down-regulation of the current (5, 14, 49).

Physiological Relevance of the Findings—This study demonstrates that point mutations upstream of the CaMBDs, such as G321S, may destabilize CaM binding, potentially weakening or abolishing the predicted self-sustaining action potential firings, promoted by CaM modulation of hKv7.4 currents in SGNs. Reduction and/or removal of the capacity to generate excitability will not only alter information coding but also reduce growth and survival of SGNs as well as survival of neurons in the cochlear nucleus (50, 51). This, conceivably, may result in progressive degeneration of upstream neurons.

Future Studies—Future studies are required to determine the effects of a local and global increase of intracellular Ca^{2+} directly in SGNs. Furthermore, it is not yet known whether the G321S mutation affects both the *a* and *b* isoforms of Kv7.4. Additionally, CaM binding to Kv7 channels regulates channel assembly (25), trafficking (52, 53), and function (5, 49). The expressions of multiple splice variants that are resistant to functional modulation by CaM may further our understanding of the regulation of Kv7 channels in native cells.

Author Contributions—C. R. S., H. J. K., R. L. W., V. Y. Y., P. C. Y., and J. X. performed the experiments. C. R. S., H. J. K., R. L. W., V. Y. Y., C. E. C., X. D. Z., N. C., and E. N. Y. designed the experiments and prepared the manuscript. All authors analyzed the results and approved the final version of the manuscript.

Acknowledgments—We thank members of our laboratory for comments on the manuscript.

References

1. Yus-Najera, E., Santana-Castro, I., and Villarroel, A. (2002) The identification and characterization of a noncontinuous calmodulin-binding site in noninactivating voltage-dependent KCNQ potassium channels. *J. Biol. Chem.* **277,** 28545–28553
2. Mooseker, M. S., and Cheney, R. E. (1995) Unconventional myosins. *Annu. Rev. Cell Dev. Biol.* **11,** 633–675
3. Tadross, M. R., Dick, I. E., and Yue, D. T. (2008) Mechanism of local and global Ca^{2+} sensing by calmodulin in complex with a Ca^{2+} channel. *Cell* **133,** 1228–1240
4. Wingo, T. L., Shah, V. N., Anderson, M. E., Lybrand, T. P., Chazin, W. J., and Balser, J. R. (2004) An EF-hand in the sodium channel couples intracellular calcium to cardiac excitability. *Nat. Struct. Mol. Biol.* **11,** 219–225
5. Gamper, N., and Shapiro, M. S. (2003) Calmodulin mediates Ca^{2+}-dependent modulation of M-type K+ channels. *J. Gen. Physiol.* **122,** 17–31
6. Wen, H., and Levitan, I. B. (2002) Calmodulin is an auxiliary subunit of KCNQ2/3 potassium channels. *J. Neurosci.* **22,** 7991–8001
7. Bushell, K. M., Söllner, C., Schuster-Boeckler, B., Bateman, A., and Wright, G. J. (2008) Large-scale screening for novel low-affinity extracellular protein interactions. *Genome Res.* **18,** 622–630
8. Schuster-Böckler, B., and Bateman, A. (2008) Protein interactions in human genetic diseases. *Genome Biol.* **9,** R9
9. Bähler, M., and Rhoads, A. (2002) Calmodulin signaling via the IQ motif. *FEBS Lett.* **513,** 107–113
10. Gamper, N., Li, Y., and Shapiro, M. S. (2005) Structural requirements for differential sensitivity of KCNQ K+ channels to modulation by Ca^{2+}/calmodulin. *Mol. Biol. Cell* **16,** 3538–3551
11. Peterson, B. Z., DeMaria, C. D., Adelman, J. P., and Yue, D. T. (1999) Calmodulin is the Ca^{2+} sensor for Ca^{2+} -dependent inactivation of L-type

calcium channels. *Neuron* **22,** 549–558
12. Dick, I. E., Tadross, M. R., Liang, H., Tay, L. H., Yang, W., and Yue, D. T. (2008) A modular switch for spatial Ca^{2+} selectivity in the calmodulin regulation of CaV channels. *Nature* **451,** 830–834
13. Maylie, J., Bond, C. T., Herson, P. S., Lee, W. S., and Adelman, J. P. (2004) Small conductance Ca^{2+}-activated K+ channels and calmodulin. *J. Physiol.* **554,** 255–261
14. Shamgar, L., Ma, L., Schmitt, N., Haitin, Y., Peretz, A., Wiener, R., Hirsch, J., Pongs, O., and Attali, B. (2006) Calmodulin is essential for cardiac IKS channel gating and assembly: impaired function in long-QT mutations. *Circ. Res.* **98,** 1055–1063
15. Barhanin, J., Lesage, F., Guillemare, E., Fink, M., Lazdunski, M., and Romey, G. (1996) K(V)LQT1 and lsK (minK) proteins associate to form the I(Ks) cardiac potassium current. *Nature* **384,** 78–80
16. Sanguinetti, M. C., Curran, M. E., Zou, A., Shen, J., Spector, P. S., Atkinson, D. L., and Keating, M. T. (1996) Coassembly of K(V)LQT1 and minK (IsK) proteins to form cardiac I(Ks) potassium channel. *Nature* **384,** 80–83
17. Neyroud, N., Tesson, F., Denjoy, I., Leibovici, M., Donger, C., Barhanin, J., Fauré, S., Gary, F., Coumel, P., Petit, C., Schwartz, K., and Guicheney, P. (1997) A novel mutation in the potassium channel gene KVLQT1 causes the Jervell and Lange-Nielsen cardioauditory syndrome. *Nat. Genet.* **15,** 186–189
18. Xu, Q., Chang, A., Tolia, A., and Minor, D.L., Jr. (2013) Structure of a Ca^{2+}/CaM:Kv7.4 (KCNQ4) B-helix complex provides insight into M current modulation. *J. Mol. Biol.* **425,** 378–394
19. Coucke, P. J., Van Hauwe, P., Kelley, P. M., Kunst, H., Schatteman, I., Van Velzen, D., Meyers, J., Ensink, R. J., Verstreken, M., Declau, F., Marres, H., Kastury, K., Bhasin, S., McGuirt, W. T., Smith, R. J., Cremers, C. W., Van de Heyning, P., Willems, P. J., Smith, S. D., and Van Camp, G. (1999) Mutations in the KCNQ4 gene are responsible for autosomal dominant deafness in four DFNA2 families. *Hum. Mol. Genet.* **8,** 1321–1328
20. Van Hauwe, P., Coucke, P. J., Ensink, R. J., Huygen, P., Cremers, C. W., and Van Camp, G. (2000) Mutations in the KCNQ4 K+ channel gene, responsible for autosomal dominant hearing loss, cluster in the channel pore region. *Am. J. Med. Genet.* **93,** 184–187
21. Beisel, K. W., Rocha-Sanchez, S. M., Morris, K. A., Nie, L., Feng, F., Kachar, B., Yamoah, E. N., and Fritzsch, B. (2005) Differential expression of KCNQ4 in inner hair cells and sensory neurons is the basis of progressive high-frequency hearing loss. *J. Neurosci.* **25,** 9285–9293
22. Xu, T., Nie, L., Zhang, Y., Mo, J., Feng, W., Wei, D., Petrov, E., Calisto, L. E., Kachar, B., Beisel, K. W., Vazquez, A. E., and Yamoah, E. N. (2007) Roles of alternative splicing in the functional properties of inner ear-specific KCNQ4 channels. *J. Biol. Chem.* **282,** 23899–23909
23. Haitin, Y., and Attali, B. (2008) The C-terminus of Kv7 channels: a multifunctional module. *J. Physiol.* **586,** 1803–1810
24. Howard, R.J., Clark, K.A., Holton, J.M., and Minor, D.L., Jr. (2007) Structural insight into KCNQ (Kv7) channel assembly and channelopathy. *Neuron* **53,** 663–675
25. Wiener, R., Haitin, Y., Shamgar, L., Fernández-Alonso, M.C., Martos, A., Chomsky-Hecht, O., Rivas, G., Attali, B., and Hirsch, J.A. (2008) The KCNQ1 (Kv7.1) COOH terminus, a multitiered scaffold for subunit assembly and protein interaction. *J. Biol. Chem.* **283,** 5815–5830
26. Kim, H. J., Lv, P., Sihn, C. R., and Yamoah, E. N. (2011) Cellular and molecular mechanisms of autosomal dominant form of progressive hearing loss, DFNA2. *J. Biol. Chem.* **286,** 1517–1527
27. André, I., Bradley, P., Wang, C., and Baker, D. (2007) Prediction of the structure of symmetrical protein assemblies. *Proc. Natl. Acad. Sci. U.S.A.* **104,** 17656–17661
28. Schwake, M., Pusch, M., Kharkovets, T., and Jentsch, T. J. (2000) Surface expression and single channel properties of KCNQ2/KCNQ3, M-type K+ channels involved in epilepsy. *J. Biol. Chem.* **275,** 13343–13348
29. Mencía, A., González-Nieto, D., Modamio-Høybjør, S., Etxeberría, A., Aránguez, G., Salvador, N., Del Castillo, I., Villarroel, A., Moreno, F., Barrio, L., and Moreno-Pelayo, M.A. (2008) A novel KCNQ4 pore-region mutation (p.G296S) causes deafness by impairing cell-surface channel expression. *Hum. Genet.* **123,** 41–53
30. Geiser, J. R., van Tuinen, D., Brockerhoff, S. E., Neff, M. M., and Davis, T. N. (1991) Can calmodulin function without binding calcium? *Cell* **65,** 949–959
31. Rohl, C. A., Strauss, C. E., Misura, K. M., and Baker, D. (2004) Protein structure prediction using Rosetta. *Methods Enzymol.* **383,** 66–93
32. Yarov-Yarovoy, V., DeCaen, P. G., Westenbroek, R. E., Pan, C. Y., Scheuer, T., Baker, D., and Catterall, W. A. (2012) Structural basis for gating charge movement in the voltage sensor of a sodium channel. *Proc. Natl. Acad. Sci. U.S.A.* **109,** E93-E102
33. Yarov-Yarovoy, V., Schonbrun, J., and Baker, D. (2006) Multipass membrane protein structure prediction using Rosetta. *Proteins* **62,** 1010–1025
34. Yarov-Yarovoy, V., Baker, D., and Catterall, W. A. (2006) Voltage sensor conformations in the open and closed states in ROSETTA structural models of K(+) channels. *Proc. Natl. Acad. Sci. U.S.A.* **103,** 7292–7297
35. Wang, C., Bradley, P., and Baker, D. (2007) Protein-protein docking with backbone flexibility. *J. Mol. Biol.* **373,** 503–519
36. Mandell, D. J., Coutsias, E.A., and Kortemme, T. (2009) Sub-angstrom accuracy in protein loop reconstruction by robotics-inspired conformational sampling. *Nat. Methods* **6,** 551–552
37. Long, S. B., Tao, X., Campbell, E. B., and MacKinnon, R. (2007) Atomic structure of a voltage-dependent K+ channel in a lipid membrane-like environment. *Nature* **450,** 376–382
38. Bonneau, R., Strauss, C.E., and Baker, D. (2001) Improving the performance of Rosetta using multiple sequence alignment information and global measures of hydrophobic core formation. *Proteins* **43,** 1–11
39. Hurley, K. M., Gaboyard, S., Zhong, M., Price, S. D., Wooltorton, J. R., Lysakowski, A., and Eatock, R. A. (2006) M-like K+ currents in type I hair cells and calyx afferent endings of the developing rat utricle. *J. Neurosci.* **26,** 10253–10269
40. Rüsch, A., Lysakowski, A., and Eatock, R. A. (1998) Postnatal development of type I and type II hair cells in the mouse utricle: acquisition of voltage-gated conductances and differentiated morphology. *J. Neurosci.* **18,** 7487–7501
41. Géléoc, G. S., Risner, J. R., and Holt, J. R. (2004) Developmental acquisition of voltage-dependent conductances and sensory signaling in hair cells of the embryonic mouse inner ear. *J. Neurosci.* **24,** 11148–11159
42. Lv, P., Wei, D., and Yamoah, E. N. (2010) Kv7-type channel currents in spiral ganglion neurons: involvement in sensorineural hearing loss. *J. Biol. Chem.* **285,** 34699–34707
43. Erickson, M. G., Liang, H., Mori, M. X., and Yue, D. T. (2003) FRET two-hybrid mapping reveals function and location of L-type Ca^{2+} channel CaM preassociation. *Neuron* **39,** 97–107
44. Sukhareva, M., Hackos, D. H., and Swartz, K. J. (2003) Constitutive activation of the Shaker Kv channel. *J. Gen. Physiol.* **122,** 541–556
45. Long, S. B., Campbell, E. B., and Mackinnon, R. (2005) Voltage sensor of Kv1.2: structural basis of electromechanical coupling. *Science* **309,** 903–908
46. Lu, Z., Klem, A. M., and Ramu, Y. (2002) Coupling between voltage sensors and activation gate in voltage-gated K+ channels. *J. Gen. Physiol.* **120,** 663–676
47. Rothman, J. S., and Manis, P. B. (2003) The roles potassium currents play in regulating the electrical activity of ventral cochlear nucleus neurons. *J. Neurophysiol.* **89,** 3097–3113
48. Kalluri, R., Xue, J., and Eatock, R. A. (2010) Ion channels set spike timing regularity of mammalian vestibular afferent neurons. *J. Neurophysiol.* **104,** 2034–2051
49. Ghosh, S., Nunziato, D. A., and Pitt, G. S. (2006) KCNQ1 assembly and function is blocked by long-QT syndrome mutations that disrupt interaction with calmodulin. *Circ. Res.* **98,** 1048–1054
50. Pasic, T. R., and Rubel, E. W. (1989) Rapid changes in cochlear nucleus cell size following blockade of auditory nerve electrical activity in gerbils. *J. Comp. Neurol.* **283,** 474–480
51. Roehm, P. C., Xu, N., Woodson, E. A., Green, S. H., and Hansen, M. R. (2008) Membrane depolarization inhibits spiral ganglion neurite growth via activation of multiple types of voltage sensitive calcium channels and calpain. *Mol. Cell. Neurosci.* **37,** 376–387
52. Etxeberria, A., Aivar, P., Rodriguez-Alfaro, J. A., Alaimo, A., Villacé, P., Gómez-Posada, J. C., Areso, P., and Villarroel, A. (2008) Calmodulin regulates the trafficking of KCNQ2 potassium channels. *FASEB J.* **22,** 1135–1143
53. Alaimo, A., Gómez-Posada, J.C., Aivar, P., Etxeberría, A., Rodriguez-Alfaro, J.A., Areso, P., and Villarroel, A. (2009) Calmodulin activation limits the rate of KCNQ2 K+ channel exit from the endoplasmic reticulum. *J. Biol. Chem.* **284,** 20668–20675